Ultrafast reproducible synthesis of an Agnanocluster@MOF composite and its superior visible-photocatalytic activity in batch and in continuous flow

Supporting Information

Ana Arenas-Vivo,[a] Sara Rojas,[a] Iván Ocaña,[a] Ana Torres,[a] Marta Liras,[b,*] Fabrice Salles,[c] Daniel Arenas-Esteban,[d] Sara Bals,[d] David Ávila,[e] Patricia Horcajada[a,*]

[a] Advanced Porous Materials Unit, IMDEA Energy. Av. Ramón de la Sagra 3, 28935 Móstoles-Madrid, Spain.

[b] Photoactivated Process Unit, IMDEA Energy. Av. Ramón de la Sagra 3, 28935 Móstoles-Madrid, Spain.

[c] ICGM, Univ. Montpellier, CNRS, ENSCM, Montpellier, France.

[d] EMAT and NANOlab Center of Excellence, Univ. of Antwerp, Groenenborgenlaan 171, Antwerp 2020, Belgium.

[e] Department of Inorganic Chemistry, Chemical Sciences Faculty, Complutense University of Madrid, 28040 Madrid, Spain.

* patricia.horcajada@imdea.org; marta.liras@imdea.org

Table on Contents

1. Materials and Methods.

All reagents were commercially obtained from Sigma-Aldrich (titanium(IV) isopropoxide (97%), sulfamethazine (SMT, ≥99%), 2-hydroxy-4'-(2-hydroxyethoxy)-2-methylpropiophenone (Irgacure-2959, I-2959, 98%)), Acros Organics (2-aminoterephtalic acid (H_2BDC-NH_2, 99%), silver trifluoroacetate ($AgCF_3COO$, 98%), 4-nitroaniline (4-NA, 98%), methylene blue (MB, pure)), Evonik (aeroxide® TiO_2-P25)), Chemlab (*N*,*N*-dimethylformamide (DMF, 99.5%)), Labkem (methanol (MeOH)), and TCI ($NaBH_4$ (>95%), *p*-phenylendiamine (PPD, 98%)), and used without further purification.

Physicochemical characterization. Fourier transform infrared (FTIR) spectroscopic analyses were performed in a Nicolet 6700 (Thermo Scientific, USA) infrared spectrometer with the help of an attenuated total reflectance (ATR) diamond accessory. Nitrogen isotherms were obtained at 77 K using an AutosorbQ2 (Quantachrome Instruments, USA). Previous to the measurement, samples were evacuated at 150 °C for 16 h. Specific surface area was determined by applying Brunauer, Emmett & Teller equation (BET) in the relative pressure interval p/p_0 = 0.01-0.3 (being p_0 the saturation pressure). Pore volume and pore size distribution were calculated by the non-localized density functional theory (NLDFT) and the Horvath-Kawazoe (HK) methods, respectively. Routine X-ray powder diffraction (XRPD) patterns were collected using a conventional PANalytical Empyrean powder diffractometer (PANalytical Lelyweg, Netherlands, ϑ-2ϑ) using λCu $K_{\alpha1}$, and $K_{\alpha2}$ radiation (λ = 1.54051 and 1.54433 Å). The XRPD patterns were carried out with a 2ϑ scan between 3-35° and 3-90° with a step size of 0.013° and a scanning speed of 0.1°·s^{-1}. Thermogravimetric analyses (TGA) of the activated samples (100 ºC overnight) were carried out in an SDT Q-600 thermobalance (TA Instruments, New Castle, DE, USA) with a general heating profile from 30 to 600 °C with a heating rate of 5 °C·min^{-1} under air using a flux of 100 mL·min^{-1}. Transmission electron microscopy (TEM) images were taken with a JEM 2100 (Jeol, Tokyo, Japan) with a 200 kV acceleration voltage (point resolution 0.25 nm). For sample preparation, 1 mg of sample was dispersed in 10 mL of distilled water and sonicated with an ultrasound tip (UP400S, Hilscher, Teltow, Germany) at 20% amplitude for 20 s. For observation, 1 µL of the prepared solution was dropped over a copper TEM support with a carbon mesh (lacey carbon, 300 mesh, copper, approx. grid hole size: 63 µm, TED PELLA Redding, California, USA). Particle size was monitored via counting with ImageJ software.[1] The mean particle size was statistically estimated (*n* > 630) from TEM micrographs of the AgNC@MOF under optimized synthetic conditions. High angle annular dark field-sQuantitative determination of Ag and Ti in the samples was done with inductively coupled plasma-optical emission spectrometer (ICP-OES) Optima 3300 DV (Perkin Elmer, Waltham, MA, USA; digestion with HF and HNO_3); and energy dispersive X-ray analysis (EDX) coupled to the scanning electron microscopy Hitachi TM 1000 with tungsten applying 15 keV. UV-visible spectroscopic analysis of the solids and MB aqueous solutions were run in a Perkin Elmer® Lambda 1050 UV/vis/NIR (Perkin Elmer, Waltham, MA, USA).

High performance liquid chromatography (HPLC). Different organic molecules were analyzed by HPLC: the amount of 4-NA reacted and the PPD formed, the amount of degraded SMT, as well as the released H_2BDC-NH_2 linker were determined using a reversed phase HPLC Jasco LC-4000 series system, equipped with a PDA detector MD-4015 and a multisampler AS-4150 controlled by ChromNav software (Jasco Inc, Japan). A Purple ODS reverse-phase column (5 µm, 4.6 x 150 mm, Análisis Vínicos, Spain) was employed. For the quantification of all chemical species, isocratic conditions were used. The flow rate was 1 mL·min^{-1}, and the column temperature was fixed at 298 K. In all cases, the injection volume was 30 µL. The mobile phase was based on a mixture of 50:50 MeOH:phosphate buffered solution (PBS; 0.04 M, pH = 2.5) for H_2BDC-NH_2 ligand analysis, with a retention time (rt) and an absorption maximum of 3.03 min and 228 nm, respectively. SMT was analyzed using a mixture of 35:65 acetonitrile:water, with a rt of 2.7 min and an absorption maximum of 263 nm. PPD was analyzed using a mixture of 80:20 PBS:MeOH (PBS, 0.04 M, pH = 8) with a rt of 2.5 min and an absorption maximum of 237 nm. 4-NA was analyzed using a mixture of 80:20 PBS:MeOH (PBS, 0.04 M, pH = 8) with a rt of 16 min and an absorption maximum of 380 nm.

Preparation of the phosphate buffered solution (0.04 M, pH = 2.5 and pH = 8): 0.02 mol (2.4 g) of NaH_2PO_4 and 0.02 mol (2.84 g) of Na_2HPO_4 were dissolved in 1 L of Milli-Q water. The pH was then adjusted to 2.5 with H_3PO_4 (≥ 85%) and to basic pH with NaOH 10 M.

2. HPLC conditions.

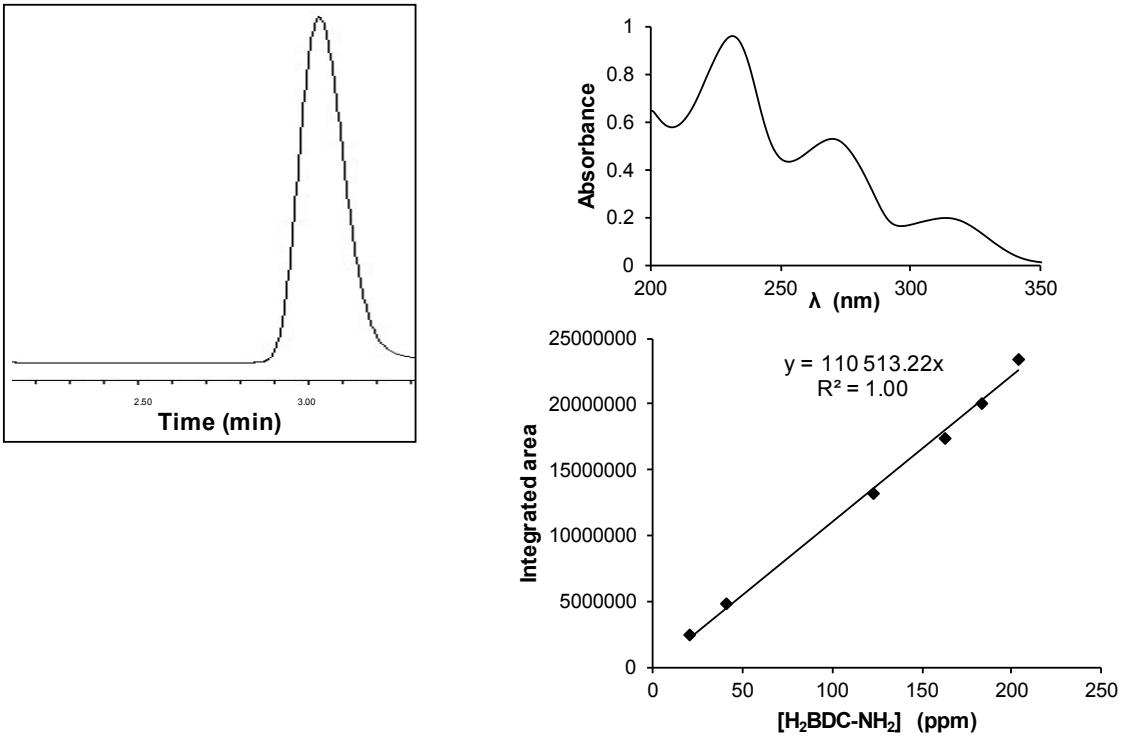

Figure S1. Calibration plot of standard by HPLC method, and UV-vis spectra and chromatogram of $H_2BDC\text{-}NH_2$.

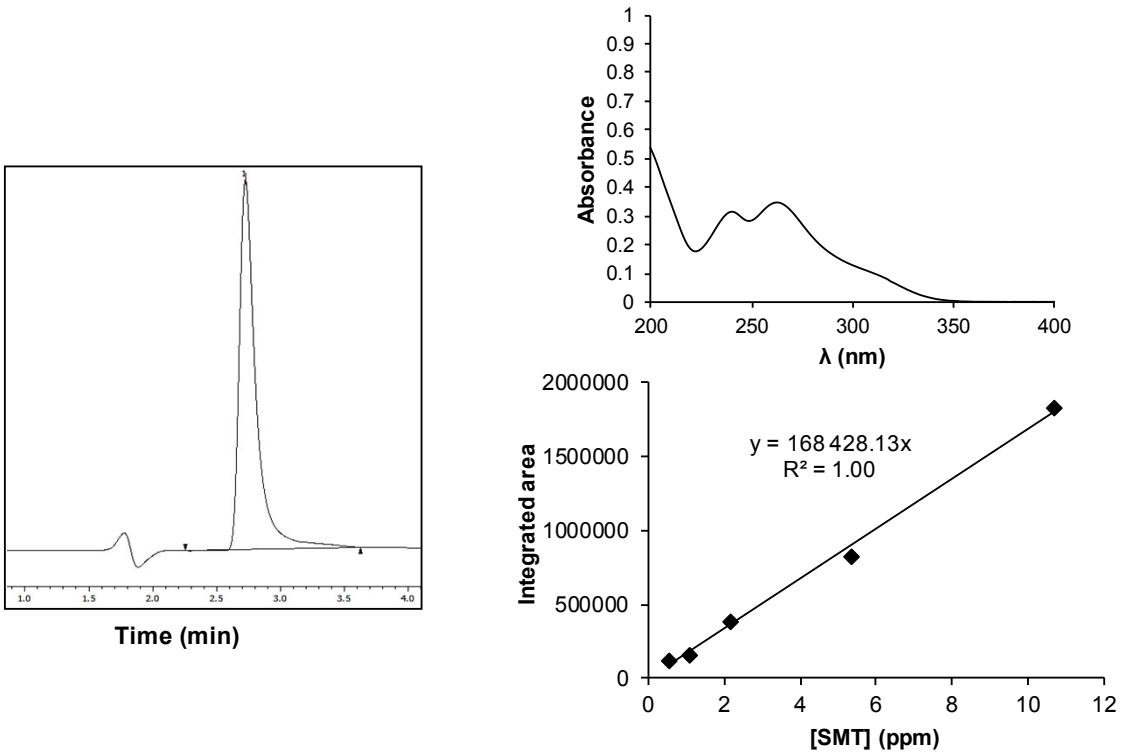

Figure S2. Calibration plot of standard by HPLC method, and UV-vis spectra and chromatogram of SMT.

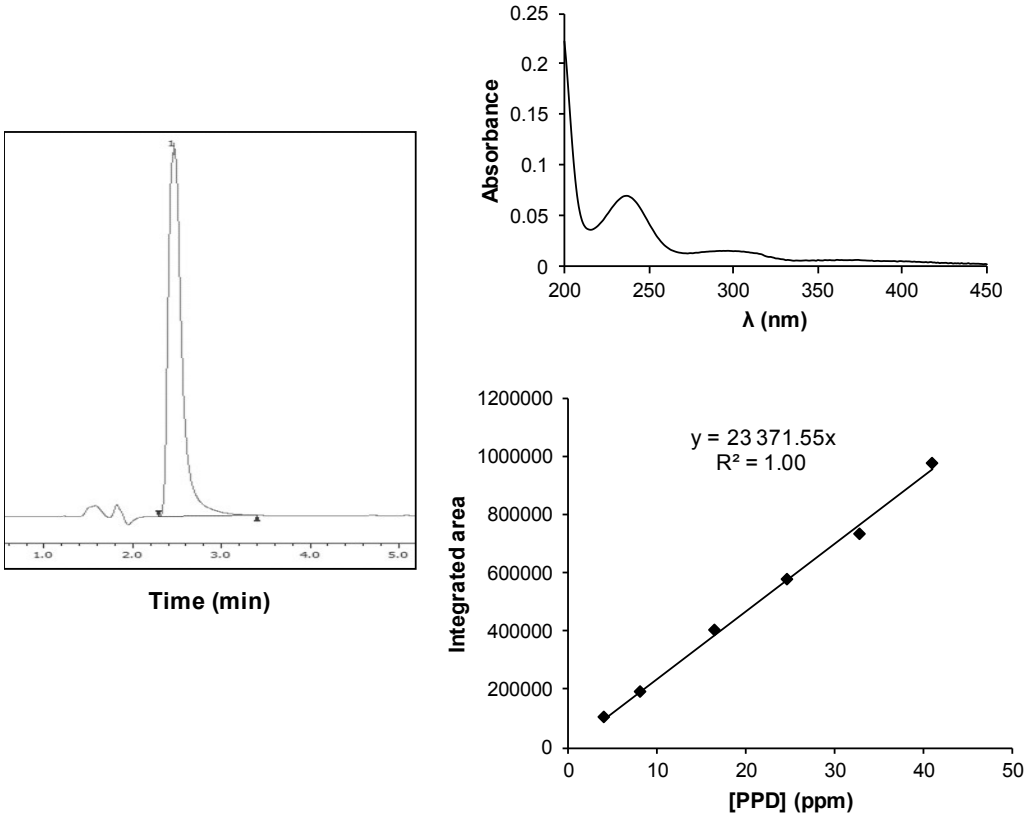

Figure S3. Calibration plot of standard by HPLC method, and UV-vis spectra and chromatogram of PPD.

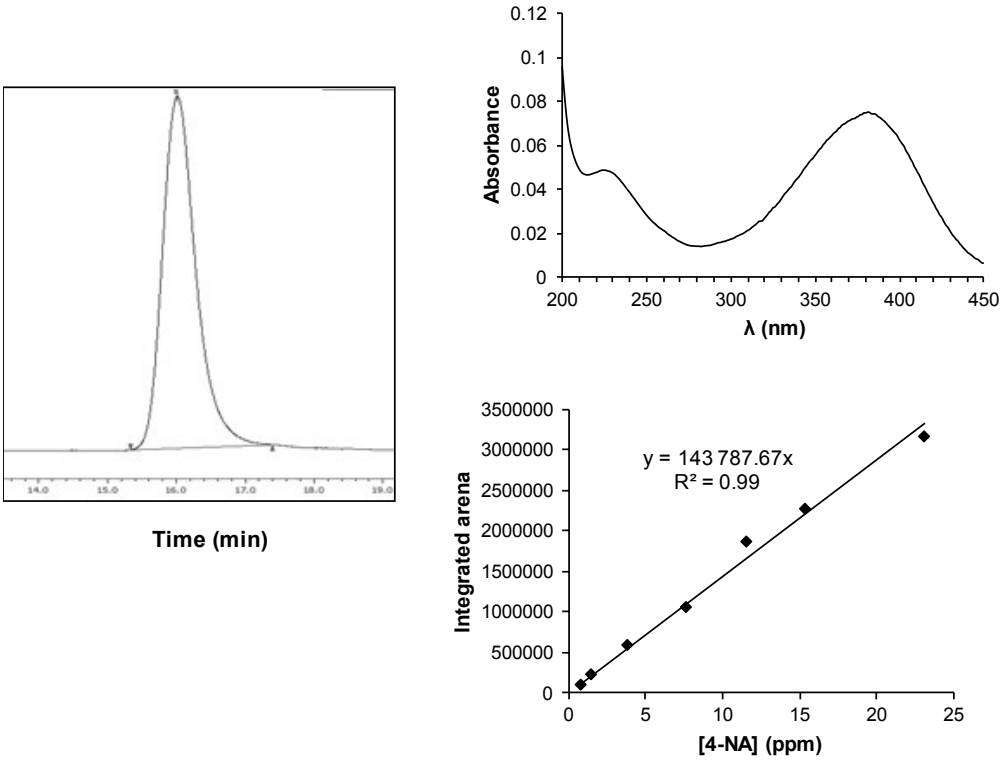

Figure S4. Calibration plot of standard by HPLC method, and UV-vis spectra and chromatogram of 4-NA.

3. Photochemical synthesis and characterization of AgNC@MIL-125-NH_2.

The synthesis of the MIL-125-NH_2 or [$Ti_8O_8(OH)_4(BDC\text{-}NH_2)_6$] was performed following a similar experimental procedure previously described.[2] In a typical synthesis, $H_2BDC\text{-}NH_2$ (76 mmol, 13.75 g) was dissolved in a mixture of 200 mL of DMF (2.5 mol) and 50 mL of MeOH (1.25 mol) at room temperature (RT) under stirring. The mixture was placed in a round bottom flask equipped with a condenser and was warmed at 373 K under air. When the mixture reached the temperature of 373 K, titanium(IV) isopropoxide (50 mmol, 15 mL) was added and then, the MilliQ water (50.56 mmol, 0.91 mL). The mixture was kept under stirring and heated at 373 K for 72 h under air. The obtained yellow solid was filtered and washed in the filter twice with 100 mL of DMF at RT. The as-synthesized solid was dispersed at RT in DMF under stirring overnight (50 mL of DMF *per* 1 g of product). Then, the same procedure was repeated twice using MeOH instead of DMF. The MIL-125-NH_2 solid was finally dried at 373 K.

The immobilization of the Ag nanoclusters (AgNCs) in the porous structure of MIL-125-NH_2 was done following the inspiration of Maretti *et al.,*[3] and Garcia-Bosch *et al.*[4] In the optimized synthesis, the previously synthetized MIL-125-NH_2 (55 mg, 0.033 mmol) and $AgCF_3COO$ (11.2 mg, 0.05 mmol, final Ti:Ag wt. ratio of 21:1) were suspended in toluene (1 mol, 80 mL) in a round bottom flask, stirred for 15 min under Ar atmosphere and protected from ambient light. In parallel, I-2959 (0.025 mmol, 5.7 mg) was solved in toluene (0.25 mol, 20 mL). After the 15 min, the I-2959 solution was added to the MIL-125-NH_2/$AgCF_3COO$ solution drop by drop. The suspension was stirred for another 5 min in dark and under Ar atmosphere. Then, the mixture was irradiated under stirring for just 15 seconds. Suspension was exposed to UV light in a photoreactor equipped with three actinic BL TL 6W/10 1FM Hg-lamps (Philips) connected in series with spectral emission in the UV region (λ_{max} = 365nm), corresponding to a total irradiance of 40 $W \cdot m^{-2}$ under 400 nm.

The obtained solid was recovered by filtration and washed with toluene (1x, 50 mL) and MeOH (4x, 50 mL). The AgNC@MIL-125-NH_2 composite was finally dried at RT and kept under darkness until use. For comparison purposes, Ag-nanoparticles@MIL-125-NH_2 (AgNP@MIL-125-NH_2) keeping the Ti:Ag proportion was also synthesized following the procedure described by some of us (see **Section S4** for full experimental procedure).[5]

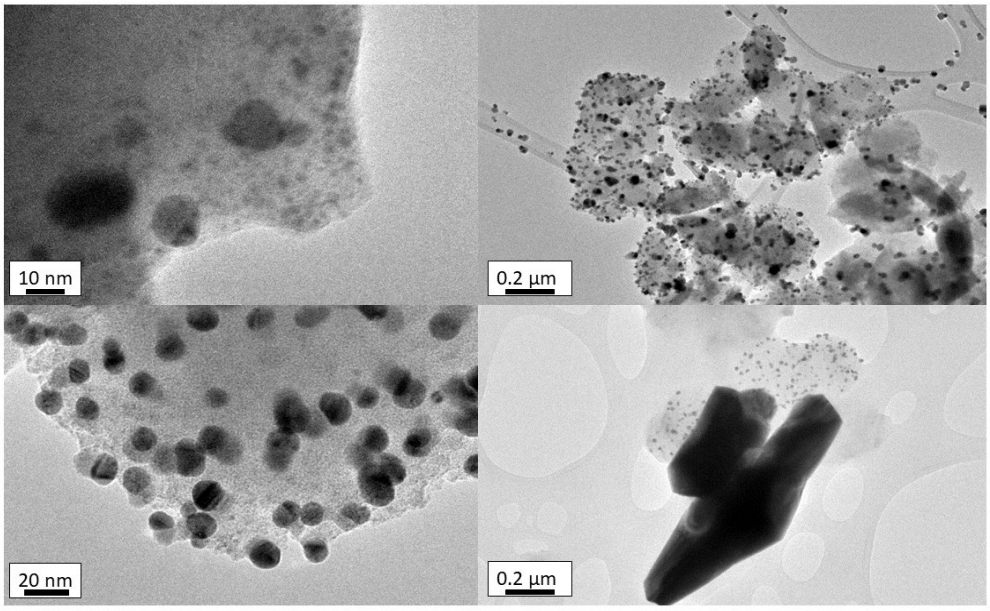

Figure S5. TEM micrographs of the AgNC@MIL-125-NH_2 analyzing the influence of photoreduction time: top, 20 min irradiation, bottom 1 h irradiation, showing some Ag microparticles with darker contrast.

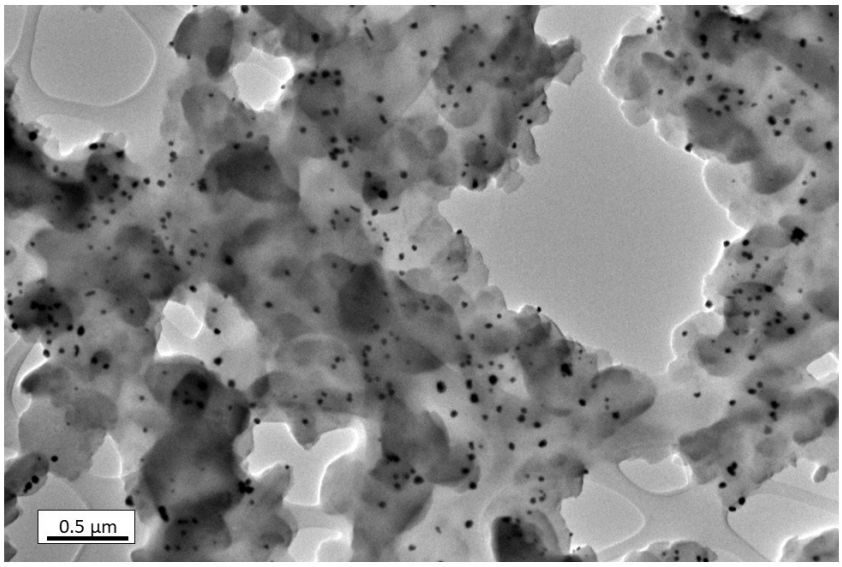

Figure S6. TEM micrographs of the AgNC@MIL-125-NH_2 analyzing the influence of the reagent addition in single step. Ag reduction was fast leading to NPs instead of NCs.

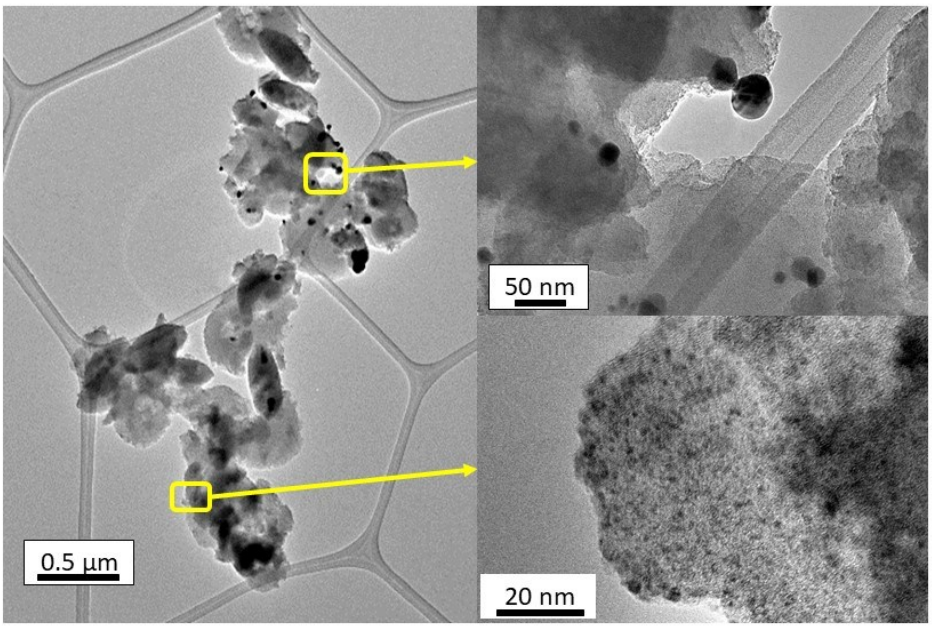

Figure S7. TEM micrographs of the AgNC@MIL-125-NH_2 in absence of stirring during photoreduction, showing heterogeneity through the sample having both AgNCs and AgNPs.

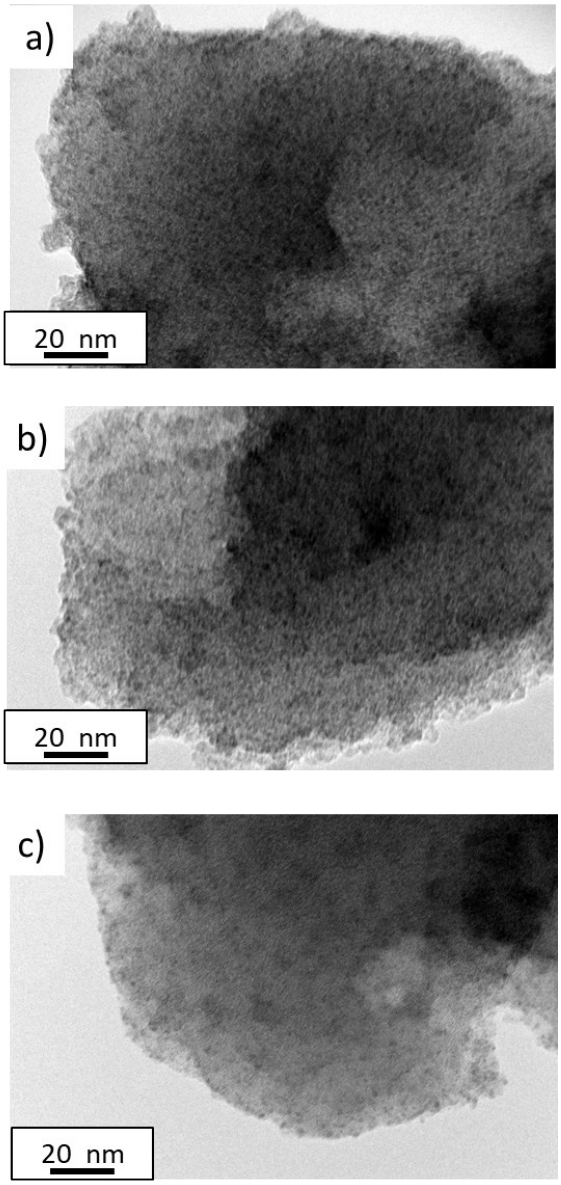

Figure S8. TEM micrographs of the AgNC@MIL-125-NH_2 showing the attainment of small AgNC with different Ti:Ag wt. ratio: a) 21:1, b) 16:1, and c) 9:1.

Table S1. Comparison of total Ag content in AgNC@MIL-125-NH_2 composites and impregnation-reduction yield with respect to the theoretically added silver, according to TGA (equipment error ± 0.2) results, with different Ti:Ag ratio

Ti:Ag (molar ratio) theoretical	**Ag (wt. %) by TGA in the AgNC@MIL-125-NH_2 composites**	**Yield (%)**
21:1	7.7	84
16:1	4.7	87
9:1	2.0	89

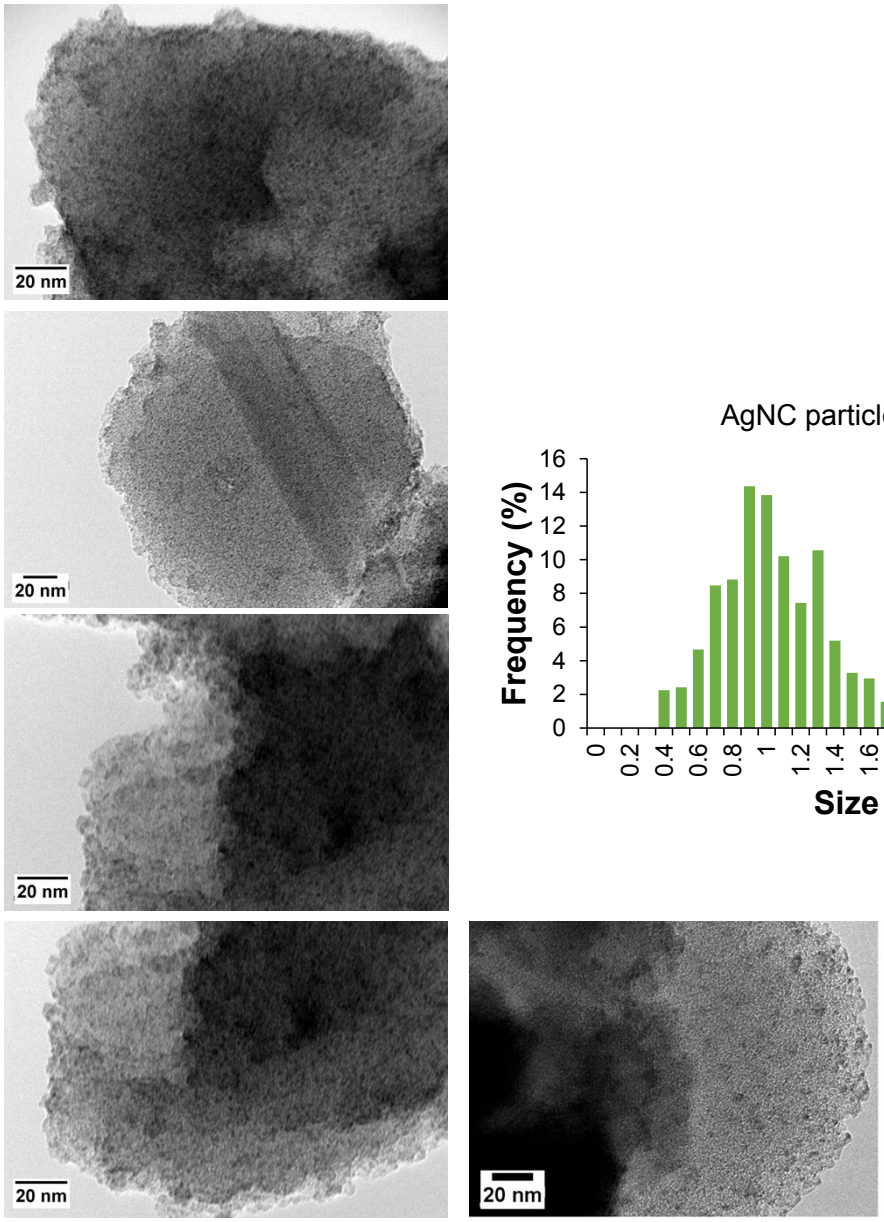

Figure S9. Histogram with the AgNCs particle size distribution in the AgNC@MIL-125-NH_2 composite, synthesized with the optimum reaction protocol as determined by TEM (N>630, from the displayed 5 images and Figure 1 d).

High angle annular dark field-scanning transmission electron microscopy (HAADF-STEM) images for tomography reconstruction were acquired using an aberration corrected "cubed" FEI Titan 60–300 electron microscope operated at 300 kV. Due to the sensitivity of these materials under a focused beam, a "fast tomography" procedure was performed, using the Fischione model 2020 single-tilt tomography holder over a tilt range from −70° to +70°, with tilt increments of 2°.[6] The reconstruction of the tilt series was performed using the Astra Toolbox 1.8 for MATLAB 2018a.3 Visualization of the 3D reconstructions was performed using the Amira 5.4.0 software. Based on a careful segmentation, it is clear that the particles are present in the pores of the MOF. See attached movie.

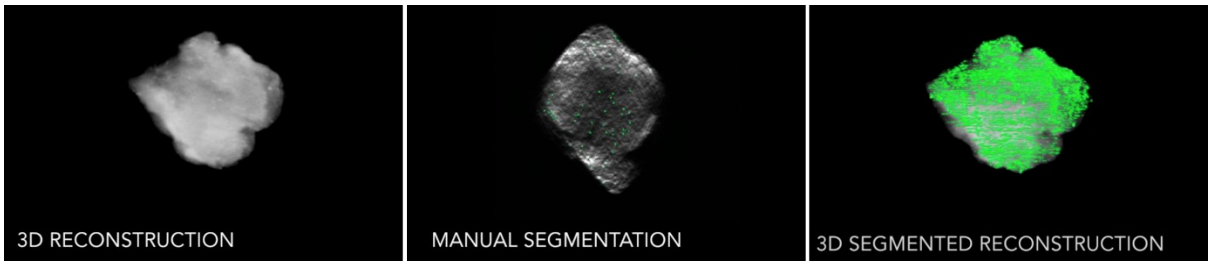

Figure S10. HAADF-STEM manual orthoslices segmentation and 3D reconstruction of AgNC@MIL-125-NH_2.

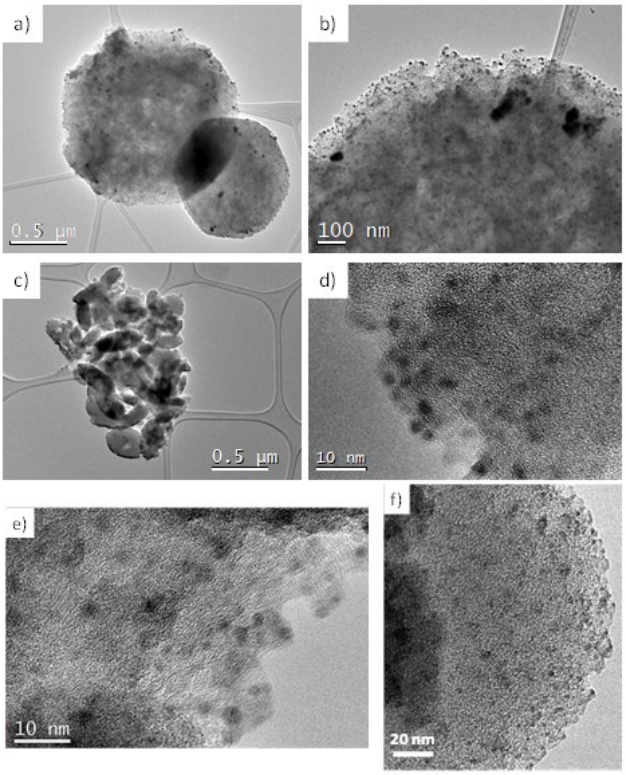

Figure S11. TEM micrographs of the AgNC@MIL-125 (a, b) and AgNC@MIL-125-NH_2 materials (c, d, e, f) at different magnifications showing the influence of the NH_2 groups in the stabilization of AgNCs.

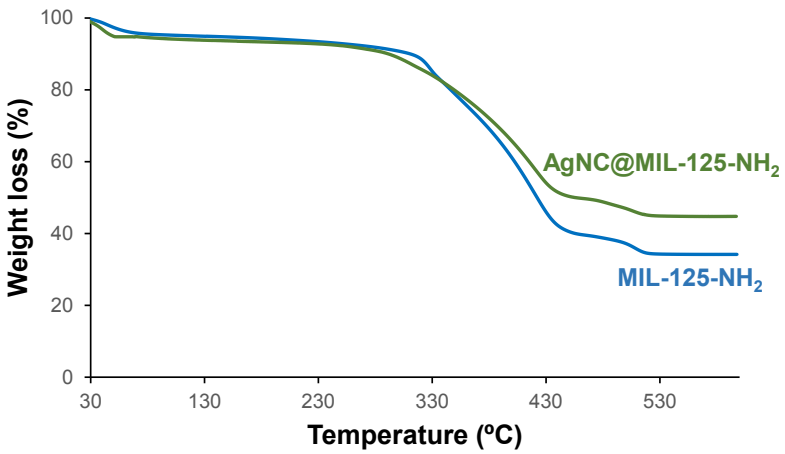

Figure S12. TGA of MIL-125-NH_2 (blue) and AgNC@MIL-125-NH_2 (green).

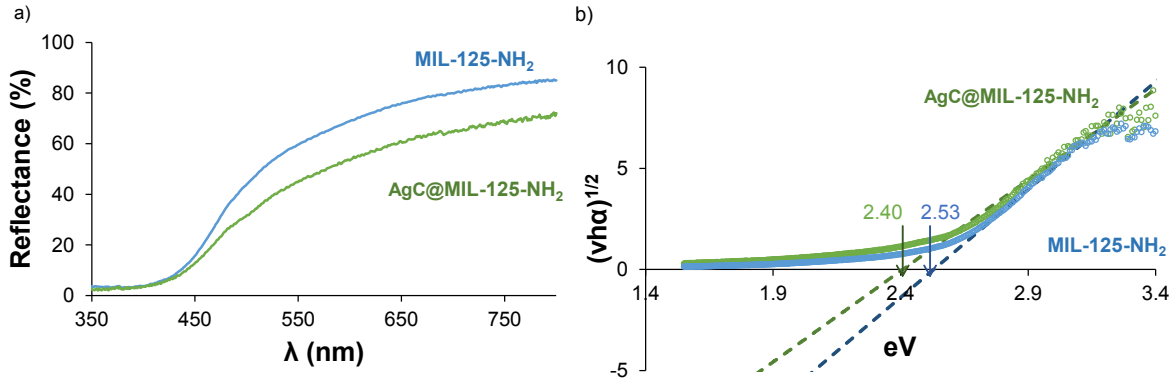

Figure S13. a) Diffuse reflectance analysis, and b) band gap estimated form the Tauc plot[7] for an indirect allowed transition of MIL-125-NH_2 (blue) and AgNC@MIL-125-NH_2 (green).

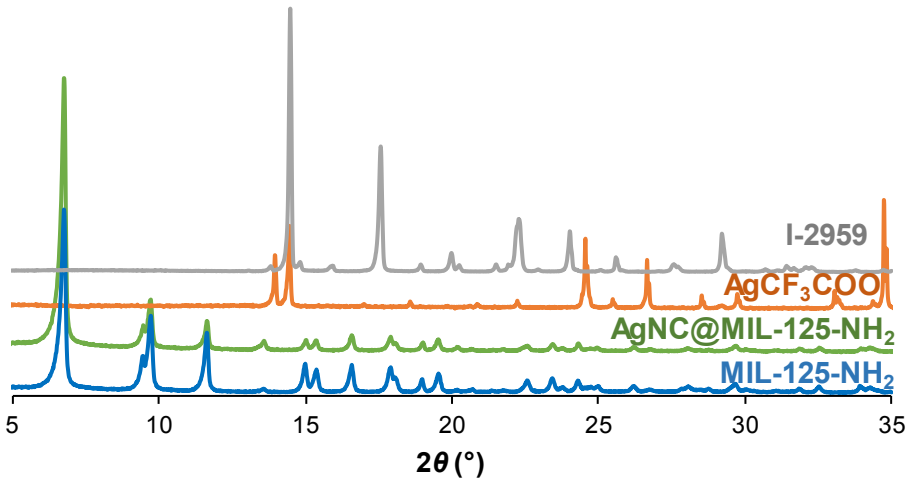

Figures S14. XRPD patterns of AgNC@MIL-125-NH_2 composite (green) compared to the pristine MIL-125-NH_2 (blue), $AgCF_3COO$ (orange), and I-2959 (grey).

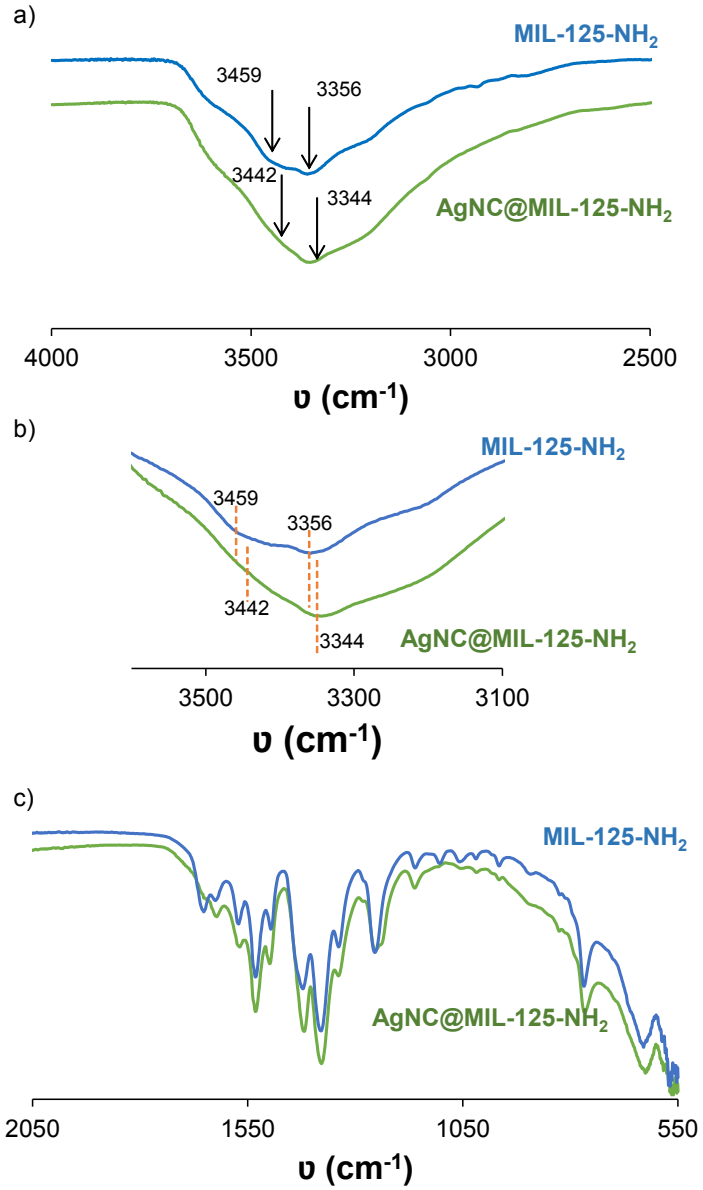

Figure S15. FTIR spectra of MIL-125-NH_2 (blue) and AgNC@MIL-125-NH_2 (green with focus for better visualization of vibrations: a) and b) on the 4000-2500 cm^{-1} region, and c) on the 2050-550 cm^{-1} region.

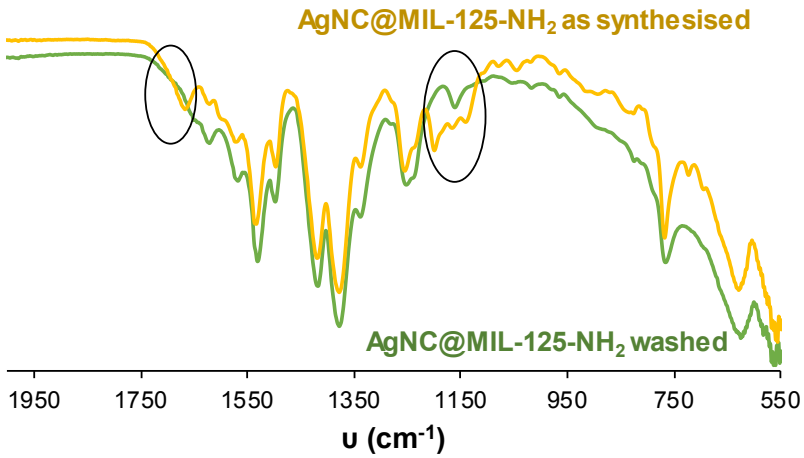

Figure S16. FTIR spectra of AgNC@MIL-125-NH_2 as-synthesized (yellow) exhibiting extra vibrations of I-2959 (black circle) and AgNC@MIL-125-NH_2 after washing (green).

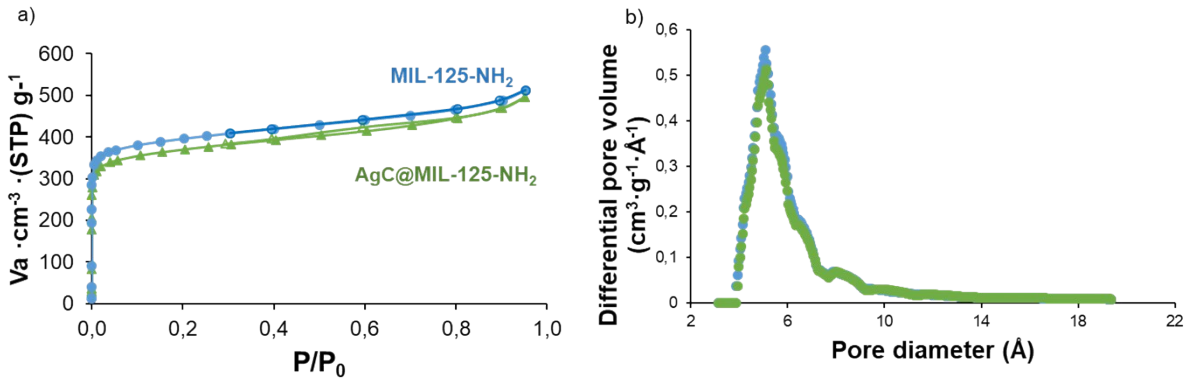

Figure S17. a) N_2 sorption isotherms, and b) pore distribution with HK method of activated MIL-125-NH_2 (blue) and AgNC@MIL-125-NH_2 (green). Solid and empty symbols indicate adsorption and desorption branches, respectively.

4. Photocatalytic degradation of emerging contaminants in water using AgNC@MIL-125-NH_2.

The photocatalytic activity of AgNC@MIL-125-NH_2 and MIL-125-NH_2 was evaluated in terms of photodegradation of emerging organic contaminants (EOCs): a) MB as model dye, and b) SMT as challenging antibiotic. MB photodegradation capacity of these materials was further compared with TiO_2 and AgNP@MIL-125-NH_2, used here as reference materials.

Synthesis of AgNP@MIL-125-NH_2: The immobilization of the Ag nanoparticles was performed following an impregnation-reduction methodology previously reported by some of us, adapted to achieve equivalent amount of silver as in the AgNCs.[5] The previously synthetized MIL-125-NH_2 (250 mg, 0.15 mmol) was dispersed in 4 mL of a 0.1 M $AgNO_3$ solution (75 mg, 0.44 mmol) in CH_3CN by sonication (2 h) and stirred at room temperature for 16 h. The silver-impregnated MOF (Ag^+@MIL-125-NH_2) was recovered by centrifugation (10000 rpm/10 min), washed with CH_3CN to remove non-attached silver precursor, and dried at 100 °C overnight. Dried Ag^+@MIL-125-NH_2 was stirred under Ar atmosphere with 2 mL of absolute ethanol. For reduction, a 2 mL absolute ethanol solution of 0.06 M $NaBH_4$ (4.5 mg, 0.12 mmol) was added to the previous ethanol mixture dropwise and stirred for 10 min under Ar atmosphere. The composite AgNP@MIL-125-NH_2 was then recovered by centrifugation (10000 rpm/10 min), thoroughly washed with absolute ethanol, and dried at 100 °C.

These photocatalytic experiments were performed in a photoreactor equipped with a 300 W Xe lamp (Oriel Instruments OPS-A500) under open air at RT, with the samples stirred and placed at a fixed distance of 21 cm from the irradiation source. A 420 nm cutoff filter (Newport 20CGA-420 IJ342) was placed between the sample and the light source to eliminate the UV irradiation. It must be pointed that prior to irradiation it is not necessary to stir the suspension until the adsorption-desorption equilibrium is reached. All experiments were performed at least in triplicate to ensure statistically reliable results. The crystallinity of all the remaining solids was analyzed by XRPD. First, the stability of MB and SMT was studied under Vis light. It was verified that MB was not degraded (after 2 h, longer time than the experimental) and neither SMT (after 24 h) under Vis light irradiation.

a) MB

In a typical experiment, 5 mg of catalyst (TiO_2, AgNC@MIL-125-NH_2, AgNP@MIL-125-NH_2 or MIL-125-NH_2) was added to 10 mL of a MB (200 ppm, in the range of textile wastewater)[8] aqueous solution (tap water) in a 20 mL vial. Photodegradation reactions were performed under continuous stirring. At certain intervals (0, 5, 10, 20, 30, 40, 50, and 60 min), an aliquot of 250 µL was collected by centrifugation for analysis by UV-vis (MB) and HPLC (H_2BDC-NH_2) (**Figure S1**). In addition, dark experiments were carried out under the same reaction conditions to evaluate the MB adsorption (**Figure S18**). These experiments were performed in triplicate.

As mentioned, **Figure S21** shows that MB is not degraded under 60 min of Vis light irradiation (remaining ~95% of the initial concentration), demonstrating the need of a photocatalyst for the MB degradation. TiO_2 could not be considered as an efficient photocatalyst for decontamination as it exhibits a moderate activity (remaining ~80% of MB after 60 min). As its photoactivity is limited by the minor visible light absorption (E_g = 3.00 eV), MB removal probably comes from MB adsorption on the particles (TiO_2 S_{BET} = 35 - 65 $m^2 \cdot g^{-1}$).

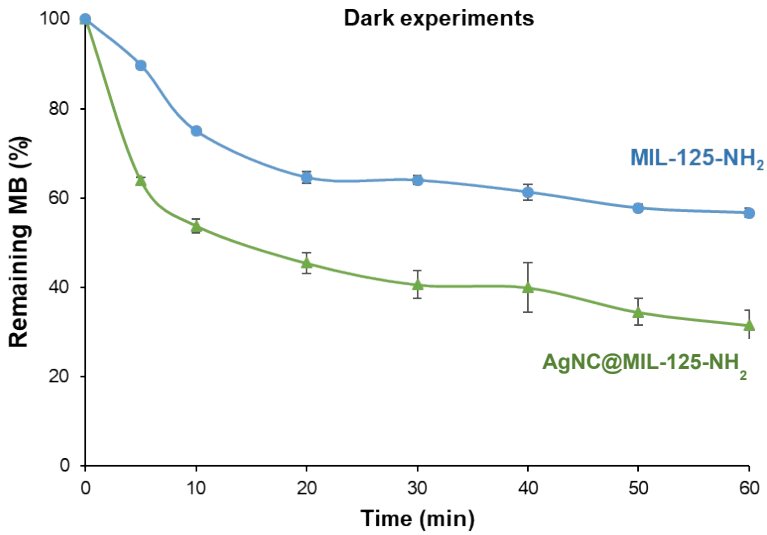

Figure S18. MB adsorption kinetics in dark using AgNC@MIL-125-NH_2 (green triangles) and MIL-125-NH_2 (blue circles).

The MB photodegradation data using AgNC@MIL-125-NH_2 and MIL-125-NH_2 were fitted to a second order kinetics according to Eqn. (1).

$$\frac{1}{[C]} = \frac{1}{[C]_0} + Kt \qquad \text{Eqn. (1)}$$

where $[C]$ and $[C]_0$ are the remaining amount of MB ($g \cdot mg^{-1}$) at the time t (min) and the initial MB concentration, respectively, and K is the second order kinetics constant ($g \cdot mg^{-1} \cdot min^{-1}$).

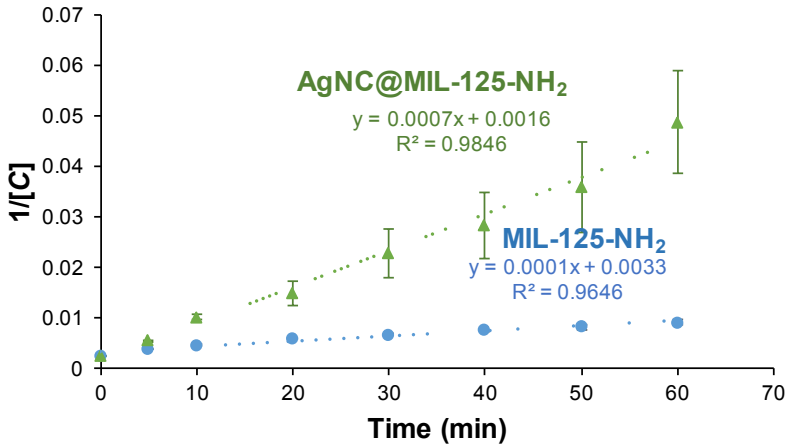

Figure S19. Fitting of MB degradation data using MIL-125-NH_2 (blue circles) and AgNC@MIL-125-NH_2 (green triangles) to a second order kinetic. Includes error bars of three replicates.

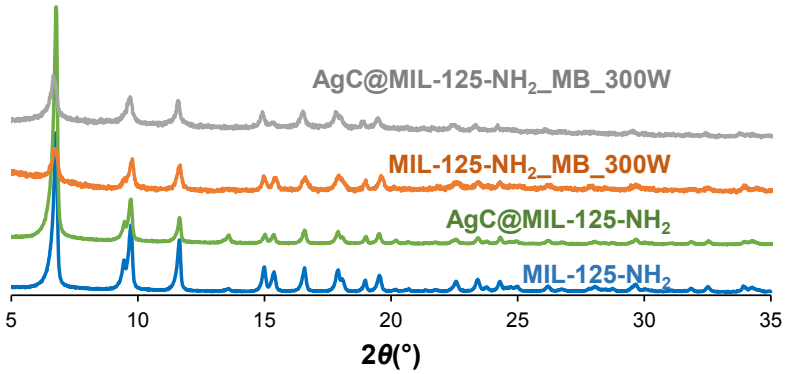

Figure S20 XRPD patterns of the MIL-125-NH_2 and AgNC@MIL-125-NH_2 before (blue and green, respectively), and after being suspended in a MB tap aqueous solution under Vis irradiation for 1 h (MIL-125-NH_2_MB_300W (orange) and AgNC@MIL-125-NH_2_MB_300W (grey)).

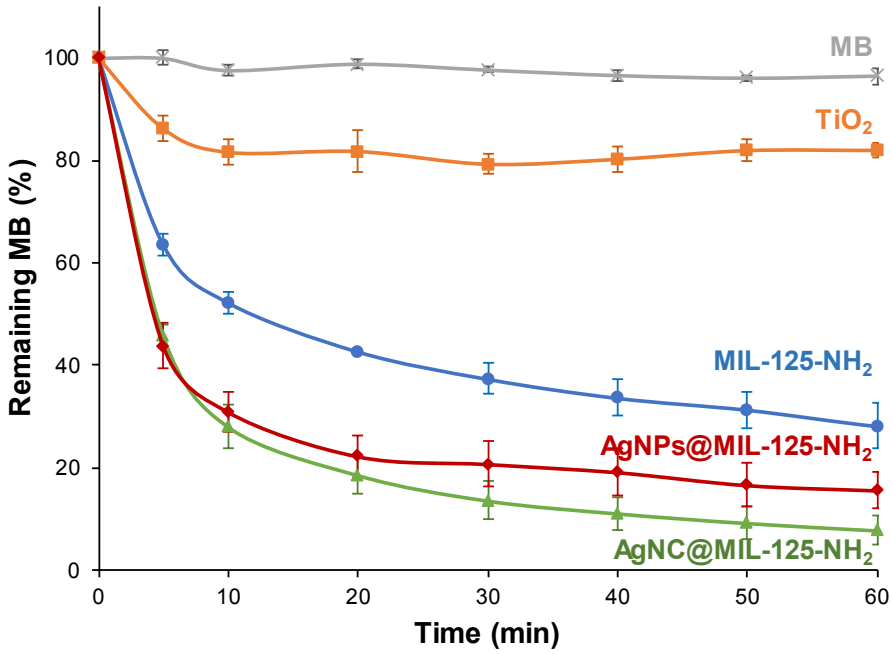

Figure S21. MB photodegradation kinetics under visible light irradiation using AgNC@MIL-125-NH_2 (green triangles) and other materials as controls: AgNP@MIL-125-NH_2 (red diamonds), MIL-125-NH_2 (blue circles), TiO_2 (orange squares), and MB control without catalyst (grey crosses).

Table S2. Comparison of degraded MB (%) using AgNC@MIL-125-NH_2 and other reported catalysts.

MOF based material	MB degraded (%)	Time (min)	Kinetic model	*K* (1^{st} in min^{-1} / 2^{nd} in $g \cdot mg^{-1} \cdot min^{-1}$)	Refs
AgNC@MIL-125-NH_2	92	60	2^{nd}	0.0007	This work
AgNPs@MIL-125-NH_2	84	60			This work
MIL-125-NH_2	72	60	2^{nd}	0.0001	This work
TiO_2	18	60			This work
HPU-4@AgBr	95	60	ND	ND	[9]
Ag-MIL-125-AC	99.5	90	Pseudo 1^{st}	0.1031	[10]
Ag_3PO_4@ MIL-125-NH_2	95	50	1^{st}	0.089	[11]
Ag_3VO_4@MIL-125-NH_2	92	15	1^{st}	0.0997	[12]
In-MOF	96	60	1^{st}	0.0621	[13]
MIL-53(Fe)	11	40	1^{st}	0.0036	[14]
Mn(dmtdc)	91	70	ND	ND	[15]
UiO-66-NH_2@ZnTCPc	68	120	Pseudo 1^{st}	0.0168	[16]
ZIF-8	83	120	Pseudo 1^{st}	0.0170	[17]
ZIF-8@Ag/AgCl	100	20	1^{st}	0.1468	[18]

ND: no data reported; AC = acetylacetone; H_2dmtdc = 3,4-dimethylthieno[2,3-b]thiophene-2,5-dicarboxylic acid; TCP = tetracarboxy phthalocyanine.

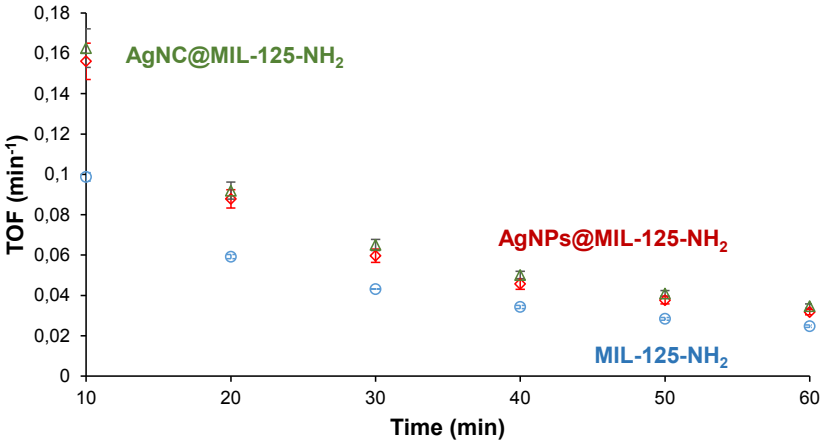

Figure S22. TOF (min^{-1}) determination of MB photodegradation using AgNC@MIL-125-NH_2 (green triangles) AgNP@MIL-125-NH_2 (red diamonds) MIL-125-NH_2 (blue circles) as catalyst.

b) SMT

In an 8 mL vial, 4 mg of AgNC@MIL-125-NH_2 or MIL-125-NH_2 were suspended in 4 mL of a SMT tap-aqueous solution (10 ppm, according with the concentration of SMT found in the environment).[19] Photodegradation reactions were performed under stirring. At certain intervals (0, 2, 5, 8, 12, 15, and 30 min), an aliquot of 100 µL was collected by centrifugation for HPLC analysis (SMT and H_2BDC-NH_2). These experiments were performed in triplicate.

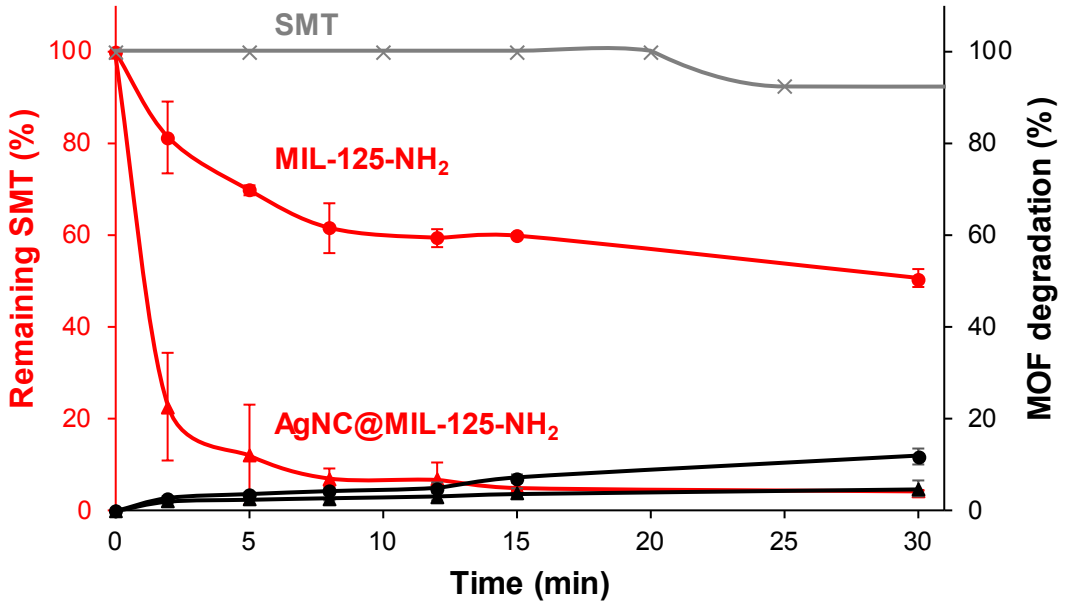

Figure S23. Effect of time on the photodegradation of SMT using MIL-125-NH_2 (red circles, left y axis) or AgNC@MIL-125-NH_2 (red triangles) as photocatalyst. SMT (grey crosses, right x axis) without catalyst is included for comparison. MOF degradation over time is also represented (in black using circles and triangles, accordingly).

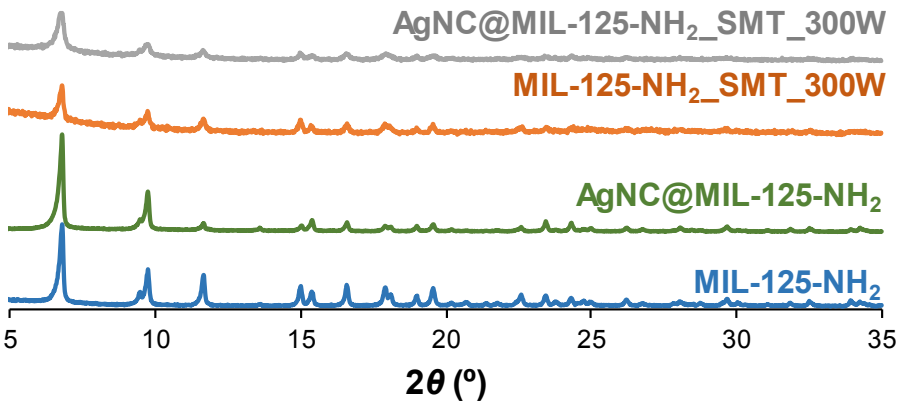

Figure S24. XRPD patterns of the MIL-125-NH_2 and AgNC@MIL-125-NH_2 before (blue and green, respectively), and after being suspended in a SMT tap aqueous solution under Vis irradiation for 30 min (orange and grey, respectively; denoted as MIL-125-NH_2_SMT_300W and AgNC@MIL-125-NH_2_SMT_300W).

To shed some light on the SMT degradation kinetics and to gain further understanding on the involved mechanism, the first 10 min of SMT degradation were fitted to a second order kinetics according to Eqn. (1).

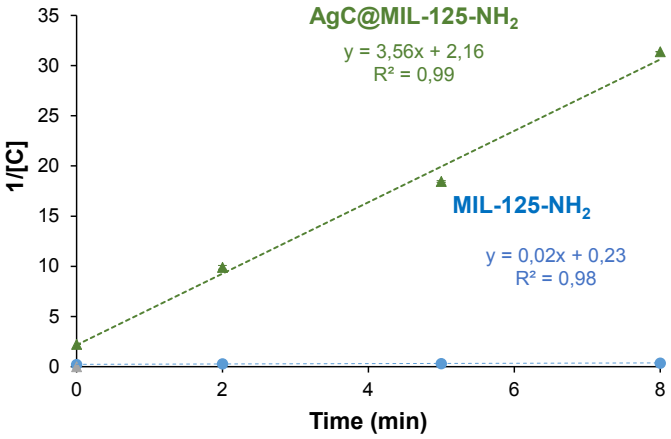

Figure S25. Fitting of SMT degradation data using MIL-125-NH_2 (blue circles) and AgNC@MIL-125-NH_2 (green triangles) to a second order kinetics.

Table S3. Comparison of degraded SMT values (% and $mg \cdot L^{-1} \cdot min^{-1}$) using AgNC@MIL-125-$NH_2$ and other MOF-based catalysts, as well as TiO_2.

MOF based material	SMT degraded, % ($mg \cdot L^{-1} \cdot min^{-1}$)	Time (min)	Kinetic model	*K* ($g \cdot mg^{-1} \cdot min^{-1}$)	Refs
AgNC@MIL-125-NH_2	96 (0.32)	30	2nd	3.56	This work
MIL-125-NH_2	49 (0.16)	30	2nd	0.02	This work
CUS@MIL-100(Fe)	100 (0.11)	180	ND	ND	[20]
PW_{12}@MFM-300(In)	98 (0.14)	120	ND	ND	[21]
MIL-53(Fe)@percarbonate	90 (83.50)	60	ND	ND	[22]
TiO_2	95 (0.08)	120	ND	ND	[23]

ND: no data reported

Continuous flow SMT photodegradation: A continuous flow reactor made of glass (length = 7.5 cm, T = 2.2 cm, volume = 10 mL) was employed to investigate SMT photodegradation through a continuous flow. In order to provide a suitable liquid and MOF distribution, before any test the reactor containing only 10 mg of AgNC@MIL-125-NH_2 powder was first conditioned with 10 mL of water (without SMT). Following the same experimental conditions as previously described at the beginning of this section, a SMT concentration of 10 $\mu g \cdot mL^{-1}$ and 21 cm between the light source and the reactor were used. Applying a NE-4000 dual-channel syringe pumping system (MicruX Technologies, Spain), a total volume of 120 mL of contaminated water were pumped into the reactor with a flow rate of 30 $mL \cdot h^{-1}$ (or *ca.* 80 $L \cdot m^{-2} \cdot h^{-1}$). The effluent was gathered at regular time intervals (10, 20, 25, 30, 35, 40, 50, 60, 70, 10, 110, 120, 130, 190, 220, and 240 min) and SMT and $H_2BDC\text{-}NH_2$ concentration was quantified to evaluate the SMT elimination and the potential MOF degradation in a continuous mode. These experiments were performed in triplicate.

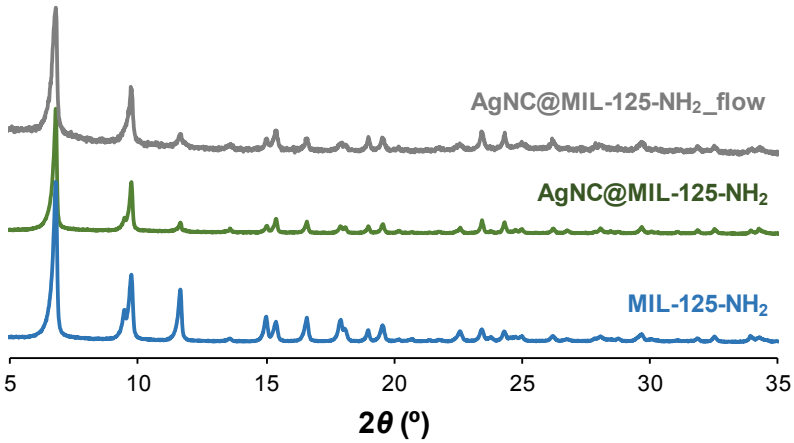

Figure S26. XRPD patterns of the AgNC@MIL-125-NH_2 before and after being used in the continuous flow reactor under Vis irradiation for 4 h.

Monte Carlo simulations. In order to determine the main preferential adsorption sites available in the titanium terephthalate MIL-125-NH_2 structure for SMT guest molecules, force field-based Monte Carlo simulations were performed. For that purpose, the Metal-Organic Framework (MOF) crystal structure was taken from the literature and geometry-optimized.[24] Partial charges in the solid were then calculated using electronegativity equalization method,[25] while Lennard Jones parameters were taken from UFF to reproduce the van der Waals interactions.[26] Regarding the SMT molecules, Density Functional Theory (DFT) calculations were performed with DMol^3 to estimate the partial charges (**see Figure S28**) obtained from a geometry optimization using PW91 functional and DNP basis set and high convergence criteria and UFF was also used for Lennard-Jones parameters. The loading of the MOF by 1 or 2 SMT molecules (closed to the experimental loadings) were simulated by Monte Carlo (see **Figures S27**), using a temperature equal to 300 K, rigid solid and molecules structures and with a multi-cell (simulation box) large enough to consider a cut-off distance for Lennard Jones interactions equal to 12.5 Å. For a typical Monte Carlo calculation, $20 \cdot 10^6$ steps for both, equilibration and production processes, were used. From these calculations, it was therefore possible to extract the configuration of distribution of SMT molecules in the MOF pores and determine the plausible interactions.

After these calculations, the insertion of AgNCs in the MIL-125-NH_2 pores was investigated by Monte Carlo. For that purpose, previous structure and partial charges for MIL-125-NH_2 were used again and Ag nanoclusters (28 atoms) were considered without partial charge (Ag^0) and using UFF force field for Lennard Jones parameters. Monte Carlo simulations were performed in the same conditions than previously by imposing 7 Ag *per* unit-cell (which corresponded to the experimental Ag loading). From these calculations, it was thus possible to extract an Ag-loaded MIL-125-NH_2 and to run other calculations to study the loading of 1 or 2 SMT molecules in this new structure, following the same conditions than previously.

In each obtained structure, it was possible to calculate the textural properties (specific surface area for N_2, free pore volume), using the procedures developed by Düren *et al*.[27] (considering the center of a N_2 probe molecule rolling across the surface with a diameter equal to 3.681 Å) and Gubbins *et al*.[28] (probe size of 0 Å), respectively.

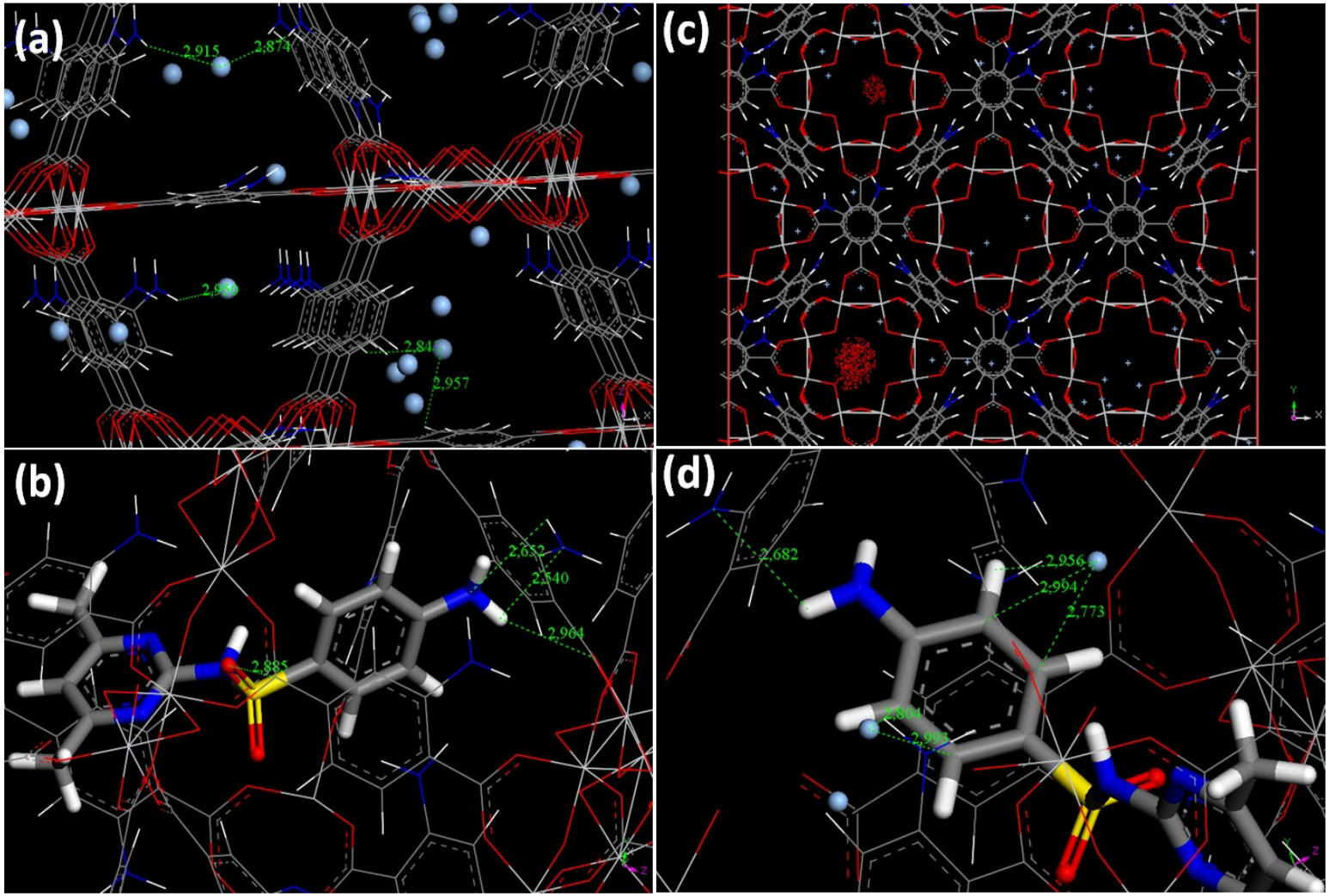

Figure S27. Plausible structures extracted from Monte Carlo simulations for (a) AgNC@MIL-125-NH_2, (b) MIL-125-NH_2 containing 1 SMT molecule, (d) AgNC@MIL-125-NH_2 containing 1 SMT molecule. Figure (c) represents the 3D-energy plot for the presence of SMT in AgNC@MIL-125-NH_2.

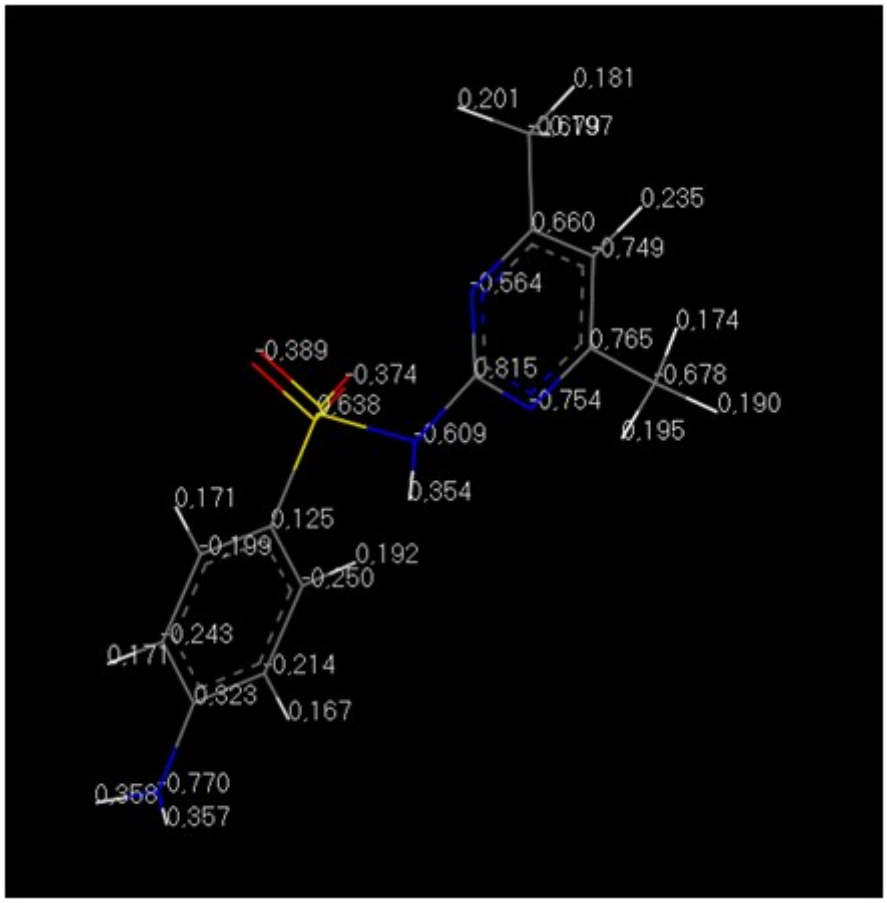

Figure S28. Partial charges extracted from DFT calculations for SMT molecules (implemented in Monte Carlo simulations)**.**

FTIR spectroscopy of SMT loaded materials

SMT-loaded materials AgNC@MIL-125-NH_2_SMT and MIL-125-NH_2_SMT were prepared by suspending 4 mg of AgNC@MIL-125-NH_2 or MIL-125-NH_2 into 4 mL of a SMT aqueous solution (10 ppm), following the same procedure as in the photodegradation experiments. The suspensions were kept under dark during all the experiment. After 24 h, the solids were centrifuged and recovered. The FTIR spectra of the SMT-loaded MIL-125-NH_2 confirmed a shift (from 3360 to 3376 cm^{-1} for the AgNC@MIL-125-NH_2; and from 3349 and 3446 cm^{-1} to 3386 and 3497 cm^{-1} for the MIL-125-NH_2, corresponding to the stretching ν_{asym}(N-H) and ν_{sym}(N-H) vibration bands of the –NH_2 groups in the MOF structure, respectively). These bands shift suggests the formation of interactions between SMT moieties and the –NH_2 group of MIL-125-NH_2. Additionally, in the case of the pristine MIL-125-NH_2, there is a shift associated to the carboxylate group found in the range of 1520-1650 cm^{-1} and 1280 to 1400 cm^{-1} for the ν_{asym} and ν_{sym} vibration bands, there is a red and blue shifts from 1534 to 1553 and 1339 to 1316 cm^{-1}, respectively. These variations are not found in the AgNC@MIL-125-NH_2 material, confirming the predictions of the simulation studies.

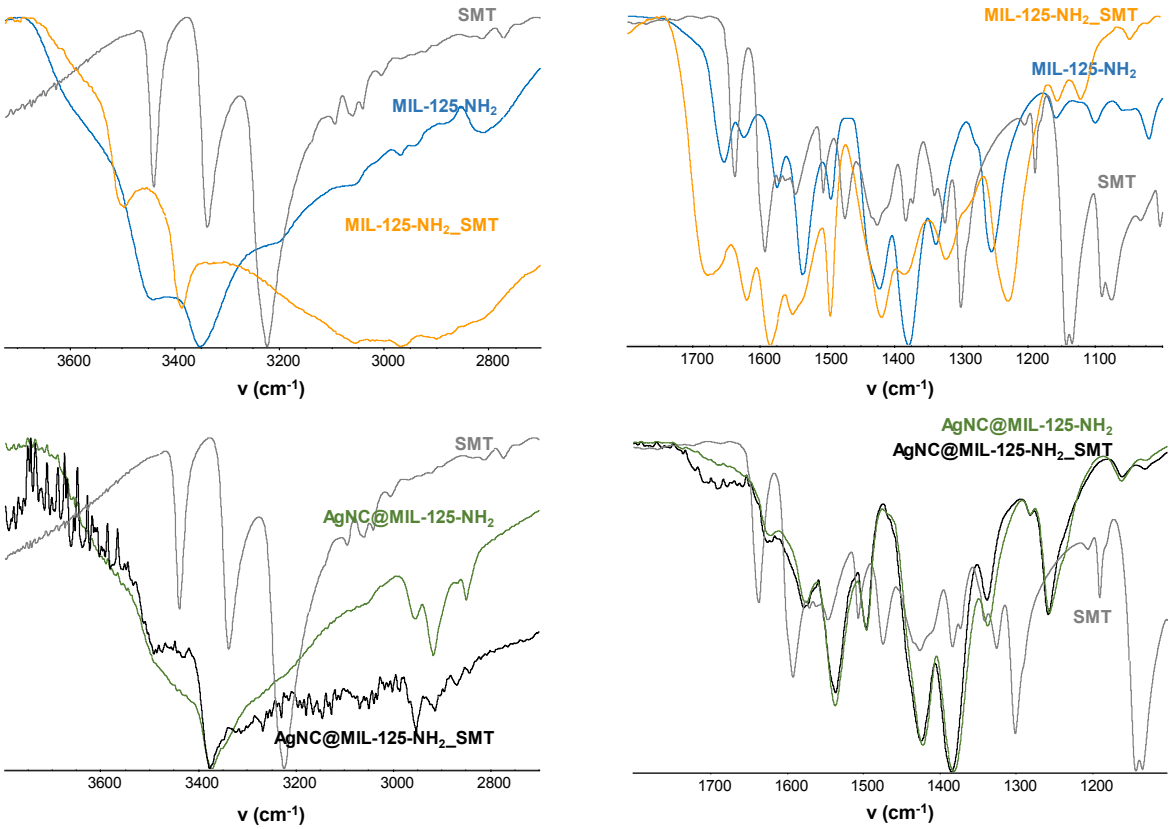

Figure S29. FTIR spectra of the MIL-125-NH_2 (blue) and AgNC@MIL-125-NH_2 (green), and their corresponding SMT (MIL-125-NH_2_SMT (orange) and AgNC@MIL-125-NH_2_SMT (black)) loaded materials. The spectrum of free SMT has been included for comparison. All solids were previously dried overnight.

The breakthrough curve shape and breakthrough times are considered as the main factors to investigate the efficiency of the continuous flow reactors. Predictions of the breakthrough curve for the effluent is a requisite for the accurate design of a continuous contaminant elimination column.[29] The column data were fitted to the Thomas model (Origin Pro 2019b software was used for non-linear curve fitting). This model is one of the most general and widely used theoretical methods to describe column performance and its described following Eqn. (2)

$$\ln\left(\frac{Co}{Ct}-1\right)=\frac{K_{Th}q_oM}{F}-K_{Th}Cot \qquad \text{Eqn. (2)}$$

where *Co* is the inlet SMT concentration (mg·L^{-1}); *Ct* is the effluent SMT concentration at time (mg·L^{-1}); K_{Th} is the Thomas rate constant (mL·mg^{-1}·min^{-1}); q_o is the equilibrium of SMT uptake (mg·g^{-1}); *M* is the mass of the absorbent (g); *F* is the inlet flow rate (mL·min^{-1}); and *t* is the flow time (min).

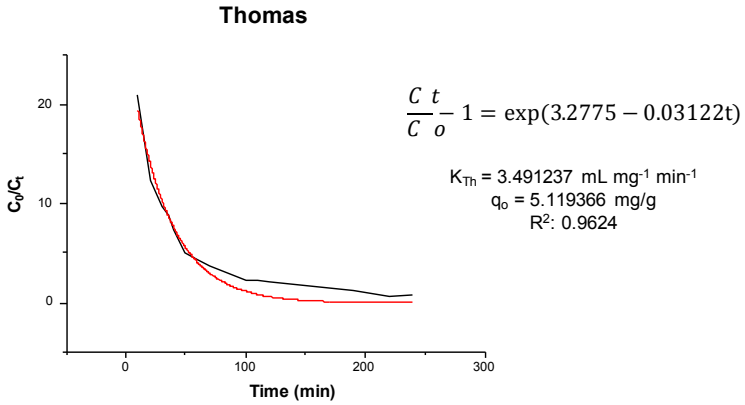

Figure S30. Breakthrough curve (red) and fitting (black) of the data from the continuous water purification studies using the Thomas models at 298 K.

5. Catalytic hydrogenation of 4-nitroaniline using AgNC@MIL-125-NH_2.

In a typical experiment, 5 mg of AgNC@MIL-125-NH_2 or MIL-125-NH_2 were added to 15 mL of 4-NA in a tap water solution (2 mM), followed by the injection of 3.5 mL of a $NaBH_4$ aqueous solution (0.1 M). These tests were performed in dark and sealed to prevent H_2 loses. At certain intervals (0, 5, 10, 15, 20, and 30 min), an aliquot of 300 µL was filtered with a syringe filter (200 nm) and collected for analysis by HPLC (4-NA, *p*-phenylendiamine-PPD, and H_2BDC-NH_2). These experiments were performed in triplicate. The 4-NA degradation kinetics data during the first 30 min were fitted to a first order kinetics according to Eqn. (3).

$$Ln[C] = Ln[C]_0 + Kt \qquad \text{Eqn. (3)}$$

where $[C]$ and $[C]_0$ are the remaining amount of 4-NA ($g \cdot mg^{-1}$) at the time t (min) and the initial 4-NA concentration, respectively, and K is the first order kinetics constant (min^{-1}).

In a first stage, the amount of AgNC@MIL-125-NH_2 catalyst required for the reaction was optimized. For an initial concentration of 4-NA of 0.2 mM considering reaction progress after 1 min, results revealed that catalyst concentrations below 3 mg were not enough (see **Figure S31**). With only 20% of 4-NA remaining after 1 min, 5 mg of catalyst were considered as the best choice.

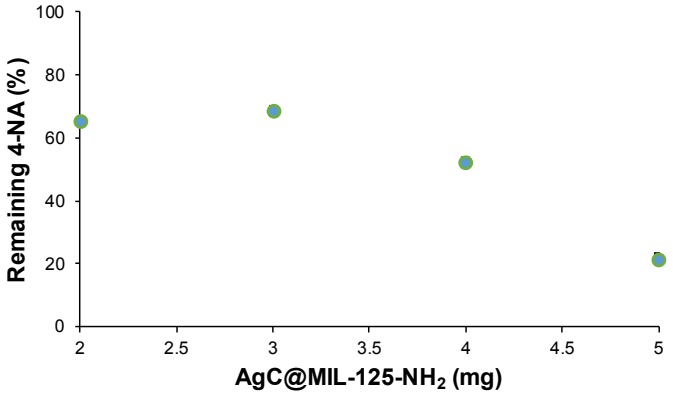

Figure S31. Selection of amount of catalyst. Hydrogenation of 4-NA 0.2 mM.

As it can be seen in **Figure S32**, reaction progress was easily followed by UV-Vis spectroscopy, by the transformation of the yellow 4-NA, with maximum absorbance at $\lambda_{4\text{-NA}}$ = 380 nm, into the uncoloured PPD with λ_{PPD} = 305 nm. As the hydrogenation catalyzed by AgNC@MIL-125-NH_2 is relatively fast, the starting concentration of the 4-NA reagent was increased up to 2 mM to better follow the reaction kinetics. In addition, for better quantification of reagents and products, as well as catalyst stability under reaction conditions, periodic aliquots of the reaction media were taken during 30 min of the reaction and quantified by HPLC. Hydrogenation reaction was also carried out under the same conditions (4-NA 2 mM, 5 mg of catalyst) using MIL-125-NH_2 as a control of the AgNC catalytic activity (see **Figure 5**).

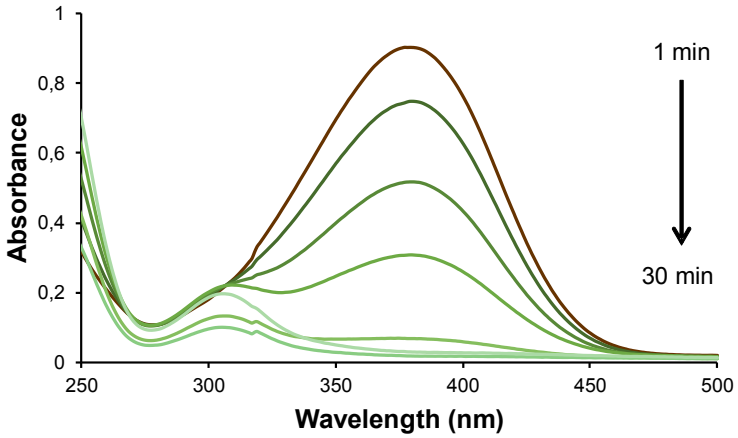

Figure S32. UV-vis spectra of the hydrogenation of 4-NA (2 mM) upon addition of AgNC@MIL-125-NH_2 catalyst.

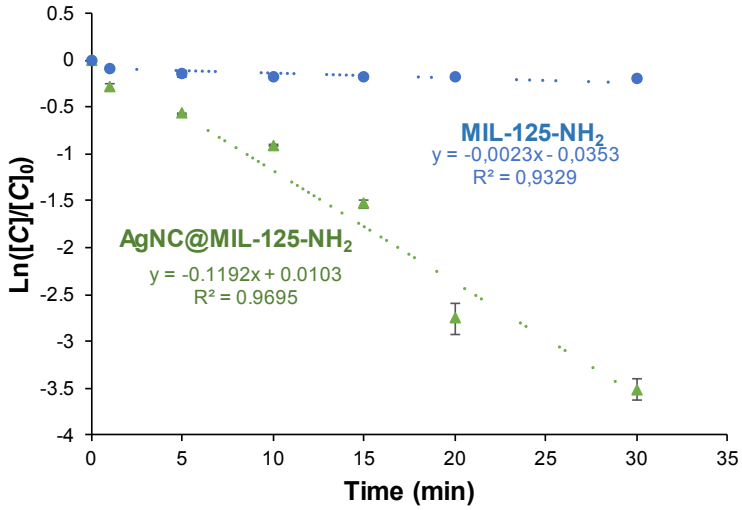

Figure S33. Fitting to a first order kinetic of 4-NA hydrogenation data using AgNC@MIL-125-NH_2 (green triangle) and MIL-125-NH_2 (blue circle) as catalyst.

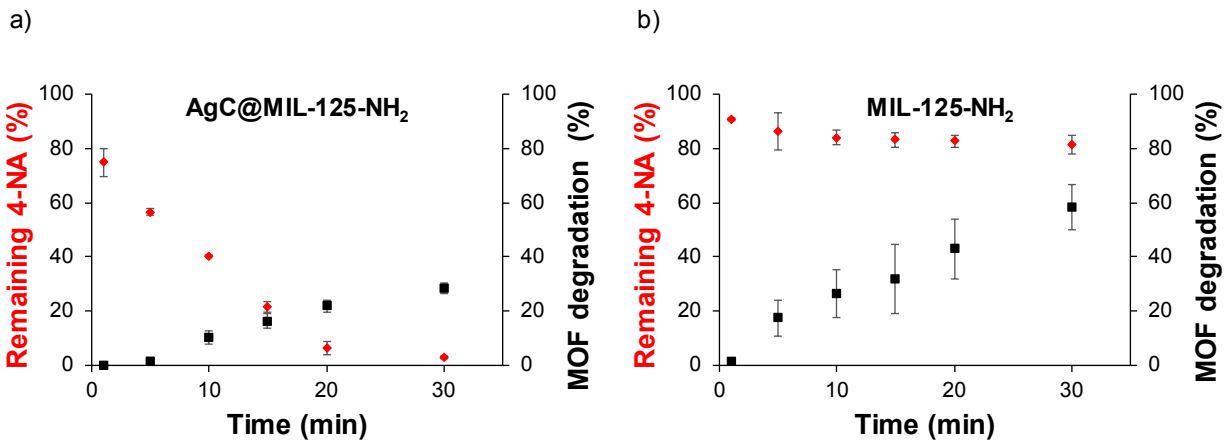

Figure S34. AgNC@MIL-125-NH_2 stability followed by HPLC: H_2BDC-NH_2 leaching (black squares) during 4-NA hydrogenation (red diamonds).

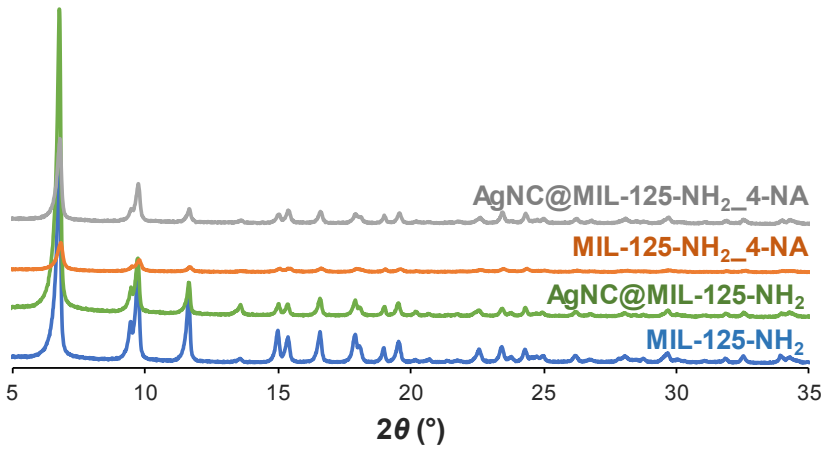

Figure S35. XRDP patterns of the MIL-125-NH_2 and AgNC@MIL-125-NH_2 before (blue and green, respectively), and after being suspended as catalyst for 4-NA hydrogenation in dark for 30 min (MIL-125-NH_2_4-NA (orange) and AgNC@MIL-125-NH_2_4-NA (grey)).

References

1 M. D. Abramoff, P. J. Magalhaes and S. J. Ram, *Biophotonics Int.*, 2004, **11**, 36–43.

2 M. A. Moreira, J. C. Santos, A. F. P. Ferreira, J. M. Loureiro, F. Ragon, P. Horcajada, P. G. Yot, C. Serre and A. E. Rodrigues, *Microporous Mesoporous Mater.*, 2012, **158**, 229–234.

3 L. Maretti, P. S. Billone, Y. Liu and J. C. Scaiano, *J. Am. Chem. Soc.*, 2009, **131**, 13972–13980.

4 N. García-Bosch, M. Liras, I. Quijada-Garrido and O. García, *RSC Adv.*, 2016, **6**, 67643–67650.

5 A. Arenas-Vivo, G. Amariei, S. Aguado, R. Rosal and P. Horcajada, *Acta Biomater.*, 2019, **97**, 490–500.

6 H. Vanrompay, A. Skorikov, E. Bladt, A. Béché, B. Freitag, J. Verbeeck and S. Bals, *Ultramicroscopy*, 2021, **221**, 113191.

7 B. D. Viezbicke, S. Patel, B. E. Davis and D. P. Birnie, *Phys. status solidi*, 2015, **252**, 1700–1710.

8 G. Nibret, S. Ahmad, D. G. Rao, I. Ahmad, M. A. M. U. Shaikh and Z. U. Rehman, in *SSRN Electronic Journal*, Elsevier BV, 2019, vol. 26–28, pp. 1959–1969.

9 H. Li, Q. Li, X. He, Z. Xu, Y. Wang and L. Jia, *Polyhedron*, 2019, **165**, 31–37.

10 R. M. Abdelhameed, M. M. Q. Simões, A. M. S. Silva and J. Rocha, *Chem. - A Eur. J.*, 2015, **21**, 11072–11081.

11 R. M. Abdelhameed, D. Maria and M. Karmaoui, *J. Photochem. Photobiol. A Chem.*, 2018, **351**, 50–58.

12 H. E. Emam, H. B. Ahmed, E. Gomaa, M. H. Helal and R. M. Abdelhameed, *J. Photochem. Photobiol. A Chem.*, 2019, **383**, 111986–111998.

13 Q. Li, D. X. Xue, Y. F. Zhang, Z. H. Zhang, Z. Gao and J. Bai, *J. Mater. Chem. A*, 2017, **5**, 14182–14189.

14 J. J. Du, Y. P. Yuan, J. X. Sun, F. M. Peng, X. Jiang, L. G. Qiu, A. J. Xie, Y. H. Shen and J. F. Zhu, *J. Hazard. Mater.*, 2011, **190**, 945–951.

15 X. D. Fang, L. B. Yang, A. N. Dou, Y. E. Liu, J. Yao, Q. Q. Xu and A. X. Zhu, *Inorg. Chem. Commun.*, 2018, **96**, 124–127.

16 Q. Liang, M. Zhang, Z. Zhang, C. Liu, S. Xu and Z. Li, *J. Alloys Compd.*, 2017, **690**, 123–130.

17 H. P. Jing, C. C. Wang, Y. W. Zhang, P. Wang and R. Li, *RSC Adv.*, 2014, **4**, 54454–54462.

18 G. Fan, J. Luo, L. Guo, R. Lin, X. Zheng and S. A. Snyder, *Chemosphere*, 2018, **209**, 44–52.

19 M. Petrovic and P. Verlicchi, *Contrib. to Sci.*, 2014, **10**, 135–150.

20 J. Tang and J. Wang, *Environ. Sci. Technol.*, 2018, **52**, 5367–5377.

21 G. Li, K. Zhang, C. Li, R. Gao, Y. Cheng, L. Hou and Y. Wang, *Appl. Catal. B Environ.*, 2019, **245**, 753–759.

22 R. Li, Z. Chen, M. Cai, J. Huang, P. Chen and G. Liu, *Appl. Surf. Sci.*, 2018, **457**, 726–734.

23 S. Fukahori and T. Fujiwara, *J. Environ. Manage.*, 2015, **157**, 103–110.

24 C. Zlotea, D. Phanon, M. Mazaj, D. Heurtaux, V. Guillerm, C. Serre, P. Horcajada, T. Devic, E. Magnier, F. Cuevas, G. Férey, P. L. Llewellyn and M. Latroche, *J. Chem. Soc. Dalt. Trans.*, 2011, **40**, 4879–4881.

25 A. K. Rappé and W. A. Goddard, *J. Phys. Chem.*, 1991, **95**, 3358–3363.

26 A. K. Rappé, C. J. Casewit, K. S. Colwell, W. A. Goddard and W. M. Skiff, *J. Am. Chem. Soc.*, 1992, **114**, 10024–10035.

27 T. Düren, F. Millange, G. Férey, K. S. Walton and R. Q. Snurr, *J. Phys. Chem. C*, 2007, **111**, 15350–15356.

28 L. D. Gelb and K. E. Gubbins, *Langmuir*, 1999, **15**, 305–308.

29 R. Han, Y. Wang, X. Zhao, Y. Wang, F. Xie, J. Cheng and M. Tang, *Desalination*, 2009, **245**, 284–297.